Applied Physics A (2023) 129:312
https://doi.org/10.1007/s00339-023-06552-x

Applied Physics A
Materials Science & Processing

Role of nitrogen partial pressure, deposition rate and annealing on stability of β-W phase

Hardepinder Singh[1] · Mukul Gupta[2] · Pooja Gupta[3,4] · Rafaela F. S. Penacchio[5] · Sergio L. Morelhao[5] · Hardeep Kumar[1]

Received: 9 January 2023 / Accepted: 6 March 2023 / Published online: 3 April 2023

Abstract

The discovery of a large Spin Hall angle in β-W makes it a potential spin–orbit torque (SOT) material for its incorporation in SOT-MRAM devices. The β-W is a metastable phase that transforms to a stable α-W phase above a certain film thickness and temperature. In this study, we report the growth of 50–70 nm thick W films prepared by nitrogen reactive sputtering at various nitrogen partial pressures in the range of 0–10% and two sputtering powers (P_W) of 30 *W* and 100 *W*. To study the thermal stability of thin films, some of the films are vacuum annealed at 200–400 °C. W films are characterized by X-ray diffraction, X-ray reflectivity and electrical resistivity measurements. The deposition rate, W film density and surface roughness tends to decrease at both the powers with an increase in nitrogen partial pressure (R_{N_2}) from 0 to 10%. XRD measurements show that at $R_{N_2} = 0\%$ the tungsten film contains mixed/pure α-W phase at 30 *W*/100 *W*, indicating the dependence of W-phase formation on the deposition power (rate). The $R_{N_2} = 2\%$ stabilizes the β-W phase at $P_W = 30$ *W*, however, higher R_{N_2} of 3% is required to stabilize β-W at $P_W = 100$ *W*. The α-W films deposited at $R_{N_2} = 0\%$ and 100 *W* are found to be stable upto 400 °C indicating the thermal stability of α-W phase. The 70 nm thick β-W films deposited at $R_{N_2} = 3\%$ and $P_W = 100$ *W* are thermally stable upto 300 °C as a majority phase with volume fraction (f_β) ~ 80%, and even at 400 °C a complete transformation to pure α-W phase is not observed.

Keywords Thin films · Reactive sputtering · Tungsten · β-W · Annealing

1 Introduction

Tungsten finds a wide array of applications ranging from diffusion barrier [1], X-ray mirror [2, 3], X-ray mask [4], fusion reactor [5, 6], the superconducting device [7], and in the field of spintronics [8–11]. Tungsten exists in two crystalline phases namely α-W and β-W [12–15]. The α-W has a body-centered cubic structure (A2) and the space group is Im $\bar{3}$ m, whereas β-W has an A15 cubic structure and the space group is Pm $\bar{3}$ n. The α-W is thermodynamically stable, while β-W is a metastable phase and observed only in the thin film form of tungsten. The β-W is stable below a critical film thickness (t_{cr}), and converts partially/completely to α-W phase at film thickness (t) higher than a critical thickness (t_{cr}) [8, 9, 16]. In general, t_{cr} increases with a decrease in deposition rate (Γ) and deposition/annealing temperature [17–20]. The β-W has captured the interest of the scientific community since the observation of a large spin Hall angle (SHA) of 0.33 by Pai et al. [8]. Recently, Chen et al. obtained the SHA of 0.65 in β-W [21], while SHA is 0.056 in Pt [22], 0.15 in β-Ta [23] and <0.07 in α-W phase [8]. Observation of large SHA in β-W makes it a potential spin–orbit torque (SOT) material for its incorporation in SOT-MRAM devices. A SOT-MRAM device consists of a magnetic tunnel junction (MTJ) heterostructure on a SOT electrode having a large SHA.

✉ Mukul Gupta
mgupta@csr.res.in

✉ Hardeep Kumar
hardeepkumar@nituk.ac.in

[1] Department of Physics, National Institute of Technology Uttarakhand, Srinagar Garhwal 246174, India

[2] UGC-DAE Consortium for Scientific Research, University Campus, Khandwa Road, Indore 452001, India

[3] Raja Ramanna Centre for Advanced Technology, Indore 452013, India

[4] Homi Bhabha National Institute, Training School Complex, Anushakti Nagar, Mumbai 400094, India

[5] Department of Applied Physics, Institute of Physics, University of São Paulo, São Paulo 05508-090, Brazil

SOT-MRAM devices could achieve much faster switching of MTJ with lower power consumption [10]. In addition to the large SHA, β-W exhibits a critical superconducting transition temperature (T_C) of 4.7 K [7] and can withstand higher upper critical magnetic fields [24]. These properties along with the observed homogeneity in β-W films make it an excellent candidate for superconducting device applications, such as superconducting nanowire single-photon detectors (SNSPD) [25, 26].

Sputtering is widely employed technique for the growth of W thin films, and sputtering parameters such as Argon gas pressure (p_{Ar}) and dc power (P_W) applied to tungsten target play an important role for the stabilization of β-W phase [17, 19, 27–29]. The β-W phase is stabilized at a lower deposition rate achieved by either relatively low P_W (3–30 *W*) or high p_{Ar} (5–100 mtorr) [17, 19, 27–29]. However, the low deposition rate leads to low manufacturing yield and is undesirable for mass scale-up production. Additionally, it is reported that high p_{Ar} leads to highly resistive β-W thin films, which is not suitable for spintronic devices.

Reactive sputtering technique employing impurity gases such as O_2, N_2 and He have been found to stabilize β-W phase [30], but O_2 is most frequently used [12, 13, 30–33]. Recent studies demonstrate that β-W phase can be stabilised using a minuscule amount of N_2 in comparison to O_2. Liu and Barmak reported the pure β-W phase in 14 nm thick W films deposited using N_2 impurity gas (6×10^{-6} to 1.2×10^{-5} torr) along with 3×10^{-3} torr of Ar gas [34]. Hon et al. reported that 1 sccm N_2 flow (along with 30 sccm Ar) was sufficient to stabilize the β-W phase, while at 2–4 sccm N_2 flow the W films become amorphous [35]. Thermal annealing (up to ~ 400 °C) is an essential step to improve the magnetic properties of spintronics devices eg. MRAM [36], however, thermal annealing may degrade the performance of SOT-MRAM device due to β-W → α-W transition in SOT layer [19, 20]. Hofer and Haberkorn reported that β-W films deposited using N_2 impurity gas under ambient conditions converts to α-W (minor W_2N phase) at an annealing temperature of 700 °C [7]. Hon et al. observed the stable β-W phase in 20 nm thick films after annealing at 300 °C [35]. However, systematic studies on the effect of temperature on β-W is missing. In literature, the β-W phase is found to be stable upto 20 nm thick films grown using nitrogen reactive sputtering at a deposition rate of 0.9–1.8 nm/min. Therefore, the aim of the present work is to carry out a systematic study on stabilizing the β-W phase in relatively thicker W films grown at a higher deposition rate, which will be beneficial for mass-scale production of β-W thin films and its integration in spintronics devices.

In the present work, we report the growth of ~ 50–70 nm thick W films prepared by nitrogen reactive sputtering at various nitrogen partial pressures in the range of 0–10% and two different dc powers applied to W target. We observed the effect of nitrogen partial pressure on the stabilization of β-W phase formation, and the effect of annealing temperature (upto 400 °C) on the stability of β-W phase.

2 Experimental

Tungsten thin films are deposited by dc reactive magnetron sputtering technique on fused silica and Si(100) substrates at ambient temperature. Film deposition is carried out at constant sputtering power (P_W) of 30 *W* and 100 *W* using Ar:N_2 gas mixture. The Ar and N_2 gases are mixed at various flow rates, but keeping the total flow rate and total pressure of the gas mixture fixed to 50 sccm and 2.8 mtorr, respectively. The partial pressure of nitrogen (R_{N_2}) in Ar:N_2 gas mixture is defined as:

$$R_{N_2}\% = \frac{p_{N_2}}{(p_{Ar} + p_{N_2})} \times 100 \quad (1)$$

where p_{Ar} and p_{N_2} are gas flow of Ar and N_2 gas, respectively. Substrates are cleaned in an ultrasonic bath using acetone followed by methanol, cleaned by running deionised water in between and finally dried using nitrogen gas. Substrates are loaded into the deposition chamber via load lock. The substrates are baked at 300 °C for 1 h in the deposition chamber to achieve a base pressure of about 1×10^{-7} torr or lower. Substrate holder is rotated at 60 rpm during film growth to ensure thickness uniformity. The deposition rate is estimated using total film thickness divided by the deposition time. Some of the films are vacuum annealed in the range of 200–400 °C (1 h) in a homemade vacuum furnace with a base pressure of about 3×10^{-6} torr.

X-ray diffraction (XRD) is used for phase analysis and quantification of β-W volume fraction. XRD measurements are carried out in θ/2θ geometry with Cu K_α radiation using a Bruker D8 Advance system. X-ray Reflectivity (XRR) measurements are performed using Cu K_α radiation with a wavelength of 1.5418 Å. XRR data is fitted using Paratt32 software to determine the thickness, density, and roughness of the films [37]. Further, the total film thickness estimated by XRR is used to calculate the deposition rate. Electrical Resistivity is measured by four-probe method using Keithley 2450 source meter.

3 Results and discussion

3.1 Effect of nitrogen partial pressure and sputtering power

Figure 1a shows the XRR spectra of W films deposited at various nitrogen partial pressure (R_{N_2}) in the range

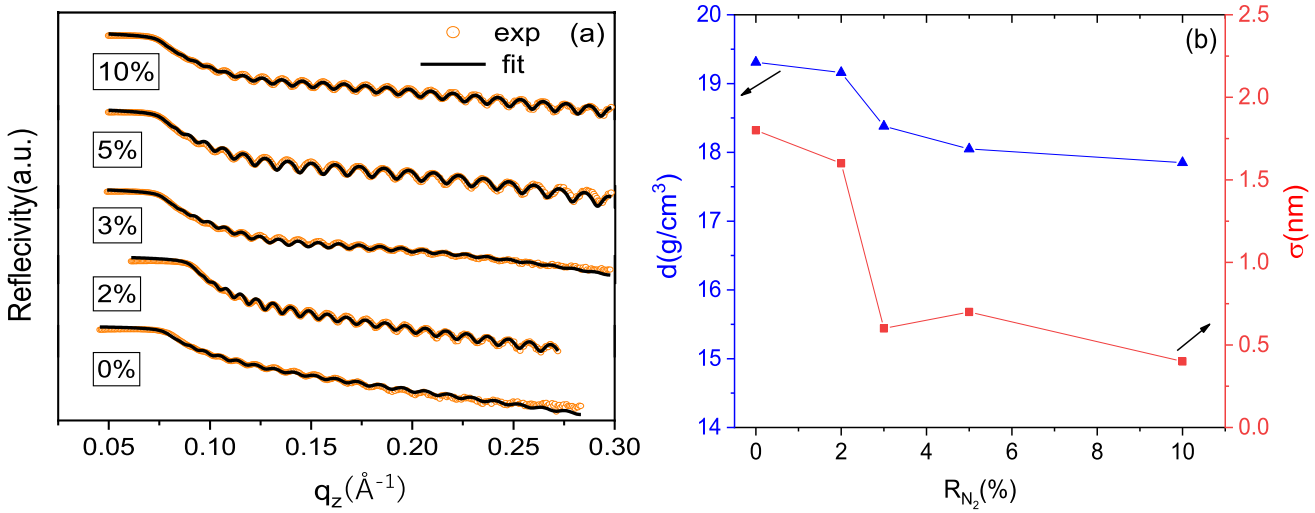

Fig. 1 **a** XRR spectra of W films deposited at $P_W = 30$ *W* and different $R_{N_2} = 0$–10%. **b** Mass density and surface roughness of W layer at $P_W = 30$ *W* as a function of R_{N_2} (%)

of 0–10% at 30 *W*. Experimental XRR data is shown by symbols and solid lines represent the fitting using Parratt formalism.

One-layer model consisting of a tungsten layer fits well with the experimental data of all films deposited at 30 *W*. However, a native oxide layer (WO_x) of 0.5–1 nm thickness is also assumed to fit the experimental data. Density of film deposited without nitrogen ($R_{N_2} = 0\%$) is 19.31 g/cm^3 and matches well with the density of bulk W (α-W). Surface roughness of W/WO_x interface is found to be 1.6 nm. Figure 1b shows the variation of the mass density of W layer and surface roughness of W/WO_x interface at $P_W = 30$ *W* as a function of the R_{N_2}(%). It is clear from Fig. 1(b) that both density and surface roughness decrease with an increase in R_{N_2}(%). Similarly, the deposition rate also found to decrease with an increase in R_{N_2}.

Estimated film thickness of W films deposited at 30 *W* is ~ 50 nm. Table 1 summarises the physical parameters extracted from XRR data along with employed film deposition parameters.

Figure 2a shows the XRR spectra of W films deposited at various nitrogen partial pressure (R_{N_2}) in the range of 0–10% at 100 *W*. One-layer model consisting of single layer of tungsten (W) fits well the experimental XRR data of films deposited at $R_{N_2} = 0$–3% and 100W, similar to films deposited at 30 *W*. However, for the films deposited at $R_{N_2} = 5$ and 10% the one-layer model does not provide a satisfactory fit of experimental data. (See Fig. S1(a) in Supplementary

Table 1 Details of sputtering power (P_W) and nitrogen partial pressure (R_{N_2}) used for the growth of W films, and film thickness (t), deposition rate (Γ), mass density (d) and surface roughness (σ) parameters derived from XRR measurements. Error in the film thickness and roughness is estimated at ± 0.05 nm. Error estimate for mass density and deposition rate is ± 0.05 g/cm^3 and ± 0.05 nm/min, respectively

Deposition parameters		Physical parameters extracted from XRR				
P_W (Watt)	R_{N_2} (%)	Layer	t (nm)	Γ (nm/min)	d (g/cm^3)	σ (nm)
30	0	W	47.9	0.96	19.31	1.8
30	2	W	45.6	0.91	19.16	1.6
30	3	W	52.2	0.87	18.38	0.6
30	5	W	44.5	0.81	18.05	0.7
30	10	W	50.4	0.77	17.85	0.4
100	0	W	66.9	3.18	19.32	1.5
100	5×10^{-7} torr*	W	66.5	3.16	19.3	1.5
100	3	W	69	3.13	18.15	1.0
100	5	W1	71.9	2.87	18.05	1.3
		W2	3.41		15.55	0.5
100	10	W1	79.9	2.66	17.91	0.6
		W2	3.64		15.55	1

*5×10^{-7} torr is the nitrogen partial pressure

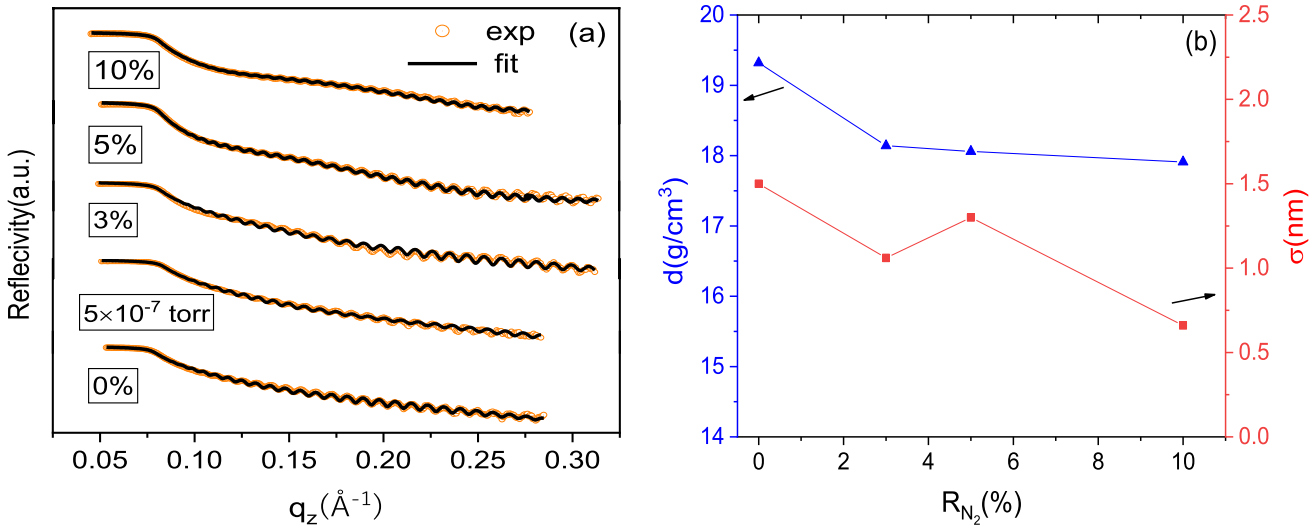

Fig. 2 **a** XRR spectra of W films deposited at $P_W = 100$ *W* and different $R_{N_2} = 0$–10%. **b** Mass density and surface roughness of W layer at $P_W = 100$ *W* as a function of R_{N_2} (%)

Information). In the one-layer model, the chi^2 value (representing the goodness of fitting) for the film deposited at $R_{N_2} = 5$ and 10% was 0.148 and 0.889, respectively.

Therefore, a two-layer model consisting of W1 and W2 layers of different density has been considered, and a satisfactory fit of experimental data is obtained (see Fig. 2a). Density of W1 and W2 layers is found to be ~ 18 g/cm^3 and 15.55 g/cm^3 for both the films, which corresponds to W and W_2N phase, respectively, from the literature [38]. The W_2N top layer may be formed due to the relatively higher R_{N_2} in these two films. It may be noted that chi^2 value (goodness of fit) in the two-layer model reduces to 0.013 and 0.006 for the film deposited at $R_{N_2} = 5$ and 10% as compared to one-layer model values (See Fig. S1(b) in Supplementary Information). Additionally, a topmost layer of native oxide (WO_x) of upto 0.5 nm on top of W (W_2N) layer in the one-layer (two-layer) model is also considered due to the surface oxidation of the films.

The variation of mass density and surface roughness of W/WO_x interface at $P_W = 100$ *W* are plotted as a function of the R_{N_2} (%) in Fig. 2b. Density of film deposited at $R_{N_2} = 0$% is found to be 19.3 g/cm^3 and matches well with density of bulk W (α-W). Variation of density, deposition rate and surface roughness of films deposited in the presence of nitrogen at 100 *W* is similar to films deposited at 30W. Estimated film thickness of films deposited at 100 *W* is ~ 70 nm. Deposition rate at 100 *W* is roughly three times the deposition rate at 30 *W*.

Figure 3a shows the XRD pattern of films deposited at 30 *W* using nitrogen partial pressure (R_{N_2}) in the range of 0–10%. The XRD pattern of the film deposited without nitrogen ($R_{N_2} = 0$%) contains two strong peaks at about 2θ ~ 35.7° and 40.4° corresponding to β(200) and α(110) reflections, respectively. Additional four peaks of very low intensity corresponding to β(211), β(400), α(211) and α(220) are also observed. This result indicates that both α and β phases coexist in the W film deposited without nitrogen.

To estimate the volume fraction of α-W(f_α) and β-W(f_β) phase, the diffraction peaks are fitted using pseudo-Voigt function after background subtraction. For this purpose the area of α(110), α(211), α(220) peaks and β(200), β(210), β(211) and β(400) peaks is taken into account. Further, it is important to mention that the peak positions of α(110) and β(210) lie very close to each other, and sometimes it may appear as a single peak with/without asymmetry. So, in that case, the peak around 40° may be fitted by a one/two pseudo-Voigt functions indicating the presence of a single/mixed phase. Following this, the experimental area of peaks is determined using the fitting and compared to theoretical areas to estimate the volume fraction of the α-W and β-W phases.

Comparison of experimental and theoretical values of peak area (refer to supplementary information) indicates that both α-W and β-W phases are highly oriented. The α-W phase is preferably oriented along the [110], while the β-W phase is preferably oriented along the [100] directions. Volume fractions of α-W and β-W phases are estimated as:

$$f_\alpha = V_\alpha/(V_\alpha + V_\beta)$$
$$f_\beta = V_\beta/(V_\alpha + V_\beta)$$

where V_α and V_β are the relative volumes of each phase and is given by

$$V_\alpha = N_\alpha v_\alpha$$

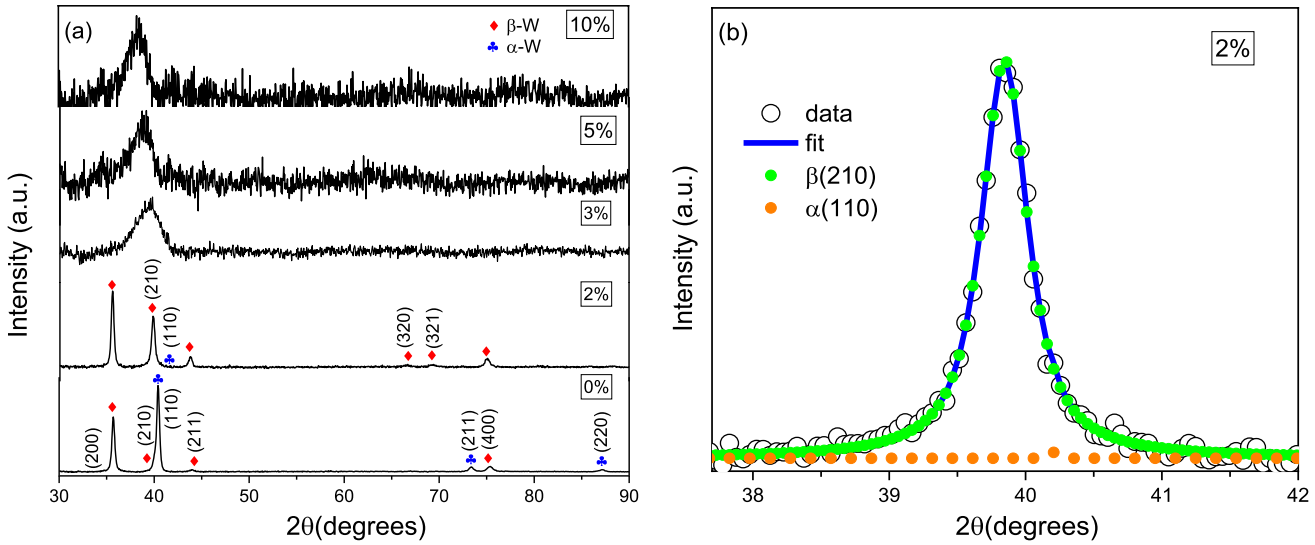

Fig. 3 **a** XRD pattern of the W films deposited at $P_W = 30$ *W* and different $R_{N_2} = 0$–10%. **b** Figure shows the fitting of peak around $2\theta = 40^o$ using double pseudo-Voigt function indicating the presence of very low intensity α(110) peak in addition to β(210) peak for the film deposited at $R_{N_2} = 2\%$

$$V_\beta = N_\beta v_\beta$$

Here, N_α and N_β are the relative number of unit cells of the α-W and β-W phases in each film and v_α and v_β are the unit cell volume of the α-W and β-W phases, respectively. The calculation of N_α and N_β has been discussed in the supplementary information. Figure 4 shows the fitted diffraction peaks of W film deposited at $P_W = 30$ *W* and $R_{N_2} = 0\%$ for the estimation of f_α and f_β. It is evident from Fig. 4 that all the peaks except the peak around $2\theta = 40^o$ could be fitted by a single pseudo-Voigt function.

In the case of films deposited at $P_W = 30$ *W* and $R_{N_2} = 0\%$, the peak around $2\theta = 40^o$ is deconvoluted to major α(110) peak at $2\theta = 40.42$ and minor β(210) peak at $2\theta = 40.03$. Using the area of all the peaks shown in Fig. 4, the f_α and f_β are estimated to be 35.5% and 64.5%, respectively. Calculated lattice parameter of α-W and β-W phase is 3.156 Å and 5.029 Å, and agrees well with the standard values (JCPDS file no. 04–0806 for α-W and JCPDS file no. 47–1319 for β-W).

As the R_{N_2} is enhanced to 2%, it is apparent from 2θ position of peaks that pure β-W phase is formed. However, during the fitting procedure of the peak at $2\theta = 40°$, the presence of a minor α-W phase is indicated by the α(110) peak at $2\theta = 40.08^o$ along with the predominant β(210) peak at $2\theta = 39.85°$. Figure 3b shows the fitting of the peak around $2\theta = 40°$. The f_α and f_β determined by fitting are 0.01% is 99.99% respectively. Thus, the adopted fitting procedure helps us to identify the presence of a very small f_α in this film, which could be underestimated otherwise. The calculated lattice parameter of β-W phase is found to be 5.069 Å which is larger than the standard value of 5.05 Å. It indicates that W lattice is expanded due to the use of nitrogen in addition to Ar in the sputtering process. Structural parameters extracted from XRD measurements are summarized in Table 2. On further increase in R_{N_2} in the range of 3–10%, only a single broad diffraction peak at about $2\theta \sim 38^o$–39^o is observed. It indicates the amorphization of the W films at relatively higher nitrogen partial pressures. Average interatomic distance for amorphous solids can be estimated using the relation $x_m = \frac{1.23\lambda}{2Sin\theta}$, where θ is the related to the center of peak and λ is the wavelength of CuK_α radiation used. The broad peak is found to shift towards a lower angle with an increase in nitrogen partial pressure, signifies the increase in interatomic distance. The calculated average interatomic distance (x_m) is 2.82 Å, 2.87 Å and 2.90 Å for $R_{N_2} = 3\%$, $R_{N_2} = 5\%$ and $R_{N_2} = 10\%$, respectively. XRD analysis of films deposited at 30 *W* indicates that nitrogen partial pressure of 2% is sufficient to stabilize β-W phase. Amorphization of W film at higher nitrogen partial pressures agrees well with the earlier reports for Nb, Fe, NiFe and W systems in literature [7, 39, 40].

Figure 5a shows the XRD pattern of films deposited at 100 *W* using nitrogen partial pressure (R_{N_2}) in the range of 0–10%. At $R_{N_2} = 0\%$, the diffraction pattern containing the peaks at $2\theta = 40.44°$, 73.43°, 87.13° could be fitted by a single pseudo-Voigt function. The peaks are indexed as α(110), α(211), and α(220), indicating the formation of a pure α-W phase in the film.

Estimated lattice parameter of α-W phase is 3.154 Å. The comparison of films deposited at 30 *W* and 100 *W* without nitrogen indicates that with an increase in dc power the β-W

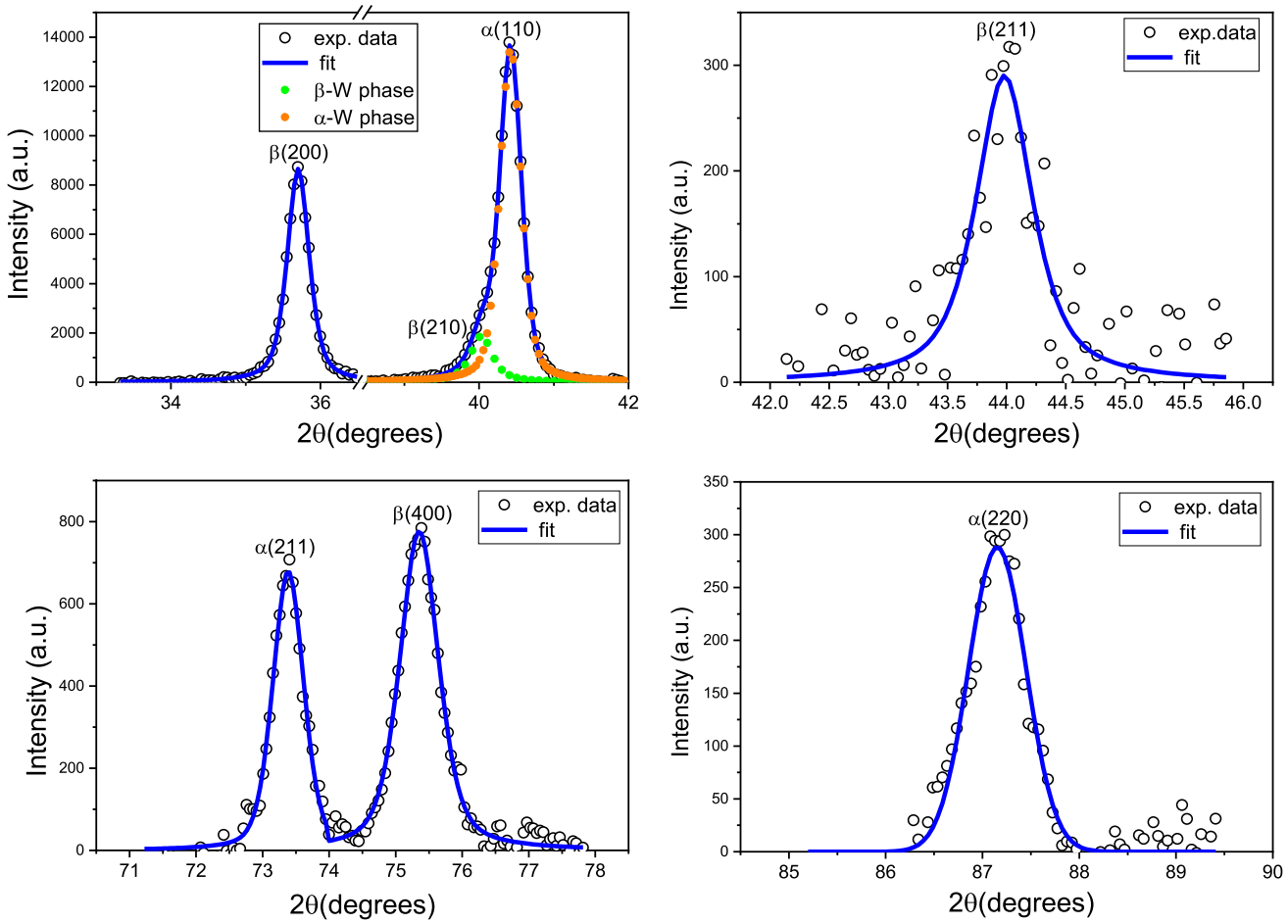

Fig. 4 Fitting of the diffraction peaks of W film deposited at $P_W = 30$ *W* and $R_{N_2} = 0\%$ for estimation of f_α and f_β

Table 2 Lattice parameter (LP), crystallite size (D), dominant phase, volume fraction of β-W phase (f_β%) estimated from XRD analysis and electrical resistivity (ρ) of all W films as a function of deposition parameters

P_W (Watt)	R_{N_2} (%)	Dominant phase, f_β%	LP (Å)	D (nm)	ρ (μΩ-cm)
30	0	β-W, 64.5 ± 1.4	5.029 ± 0.013 (β-W), 3.156 ± 0.007 (α-W)	23 ±3 (β-W), 22 ±3 (α-W)	94 ±4
30	2	β-W, 99.9 ± 3.2	5.049 ± 0.013	24 ±4	169 ±4
30	3	Amorphous	–	–	190 ±4
30	5	Amorphous	–	–	209 ±4
30	10	Amorphous	–	–	221 ±5
100	0	α-W, 0 ± 1.0	3.154 ± 0.007	22 ±3	20 ±4
100	5×10^{-7} torr*	α-W, 32.4 ± 0.8	5.034 ± 0.013 (β-W), 3.161 ± 0.007 (α-W)	24 ±4 (β-W), 19 ±2 (α-W)	66 ±4
100	3	β-W, 98.6 ± 1.9	5.059 ± 0.013 (β-W)	29 ±5	144 ±6
100	5	Amorphous	–	–	203 ±6
100	10	Amorphous	–	–	221 ±8

*5×10^{-7} torr is the nitrogen partial pressure in torr

phase transforms into α-W phase. It indicates that at higher dc power (higher deposition rate) the α-W phase is favored. To study the effect of low N_2 concentration on the type of tungsten phase formation, the 5×10^{-7} torr N_2 is introduced through the UHV leak valve. Intensity of all α-W peaks decreases and also shift toward lower angles as compared to the film deposited at $R_{N_2} = 0\%$. Additionally, the β(200) and β(400) peaks of β-W phase are observed at the introduction

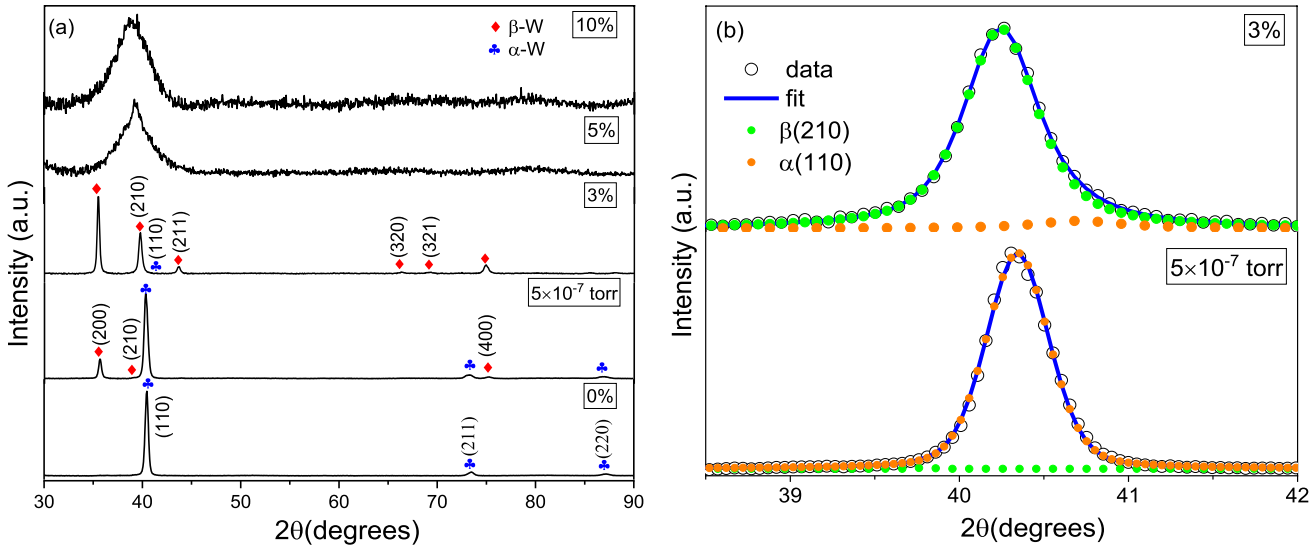

Fig. 5 **a** XRD pattern of the W films deposited at $P_W = 100$ *W* and different $R_{N_2} = 0$–10%. **b** Figure shows the fitting of peak around $2\theta = 40^o$ using double pseudo-Voigt function indicating the presence of α(110) and β(210) peak for film deposited at 5×10^{-7} torr N_2 and $R_{N_2} = 3\%$

of 5×10^{-7} torr N_2. It indicates that 5×10^{-7} torr N_2 leads to the transformation of a fraction of α-W phase to β-W phase, and thus α and β tungsten phases coexist in this film. Further, the peak around $2\theta = 40°$ could be fitted by a two pseudo-Voigt function corresponding to α(110) at 40.34° and β(210) peak at 39.8° (refer to the Fig. 5b). Estimated f_α and f_β is 67.6% and 32.4% respectively, in ~ 66 nm film deposited at 5×10^{-7} torr N_2. It signifies that 32.4% of α-W is converted to β-W phase by using a very low amount of N_2. The lattice parameter of α-W and β-W phases for this sample are found to be 3.161 and 5.034 Å, respectively.

In an earlier study by Liu and Barmak, the authors did not observe the formation of β-W phase below 10^{-6} torr N_2 in 14 nm thick films deposited at $\Gamma = 1.2$ nm/min [34]. Barmak et al. reported the growth of pure β-W films at a deposition rate of 1.8 nm/min using 1.2×10^{-5} torr N_2, but the mixed phase is observed at $\Gamma = 3.6$ nm/min with $f_\beta = 0.68$ [41]. In contrast to the above-mentioned studies, it is found that the onset of the β-W phase occurs in our case at a lower pressure of 5×10^{-7} torr N_2.

With the increase of R_{N_2} to 3%, the diffraction peaks at $2\theta = 73.26°$ corresponding to α(211) and at $2\theta = 86.95°$ corresponding to α(220) disappear. The disappearance of the α-W peaks may be due to low f_α or non-observation of α-W peaks due to film thickness constraints. However, the fitting of the peak around $2\theta = 40°$ by a two pseudo-Voigt functions indicate f_β and f_α is 98.6% and 1.4%, respectively. The lattice parameter of dominant β-W phase is found to be 5.059 Å. It is evident from Table 2 that the required nitrogen partial pressure for the stabilization of β-W phase increases from 2 to 3% as dc power is increased from 30 to 100 *W*. Application of a higher dc power to a metal target means film deposition at a higher deposition rate on the substrate. At higher deposition rate, the probability of interaction of sputtered W atoms/clusters with surrounding oxygen and nitrogen ions is lower. Therefore, at higher power higher nitrogen concentration/partial pressure is required to increase the probability of interaction between W atoms/clusters and nitrogen ions to stabilize the β-W phase. On increasing the R_{N_2} in the range of 5–10% at 100 *W*, a broad diffraction peak at about 38.5° is observed. At higher nitrogen partial pressures, the peak broadening (amorphization) is similar to that observed at 30W. It can be concluded that a limited amount of R_{N_2} is required to stabilize the β-W phase, and as R_{N_2} is increased above a limit it leads to amorphization (disorder) of the film.

Crystallite size is estimated using the Scherrer formula, $D = 0.94\lambda/\beta\cos\theta$. Here λ is the wavelength of Cuk_α radiation used (1.5418 Å), β is the full width at half maximum and θ is the diffracting angle of the highest intensity peak. Table 2 summarises the calculated values of crystallite size at various values of R_{N_2} at 30 *W* and 100 *W*. Average crystallite size of β-W phase is found to be larger than the α-W phase and agrees well with the literature [42, 43]. Larger crystallite size of β-W phase indicates the stability of the β-W phase as compared to α-W phase [44]. In most of the earlier reports, the crystallite size of α-W is found to be larger than that of β-W phase [15, 16, 20, 27], except for a few studies [42, 43]. Large crystallite size of α-W is expected due to its stable nature as compared to the metastable β-W phase [16, 44]. In films having mixed phase, the crystallite size is calculated both for α-W and β-W phases. The crystallite size was observed to be more for β-W than that of the α-W in the mixed-phase. It is reported that α-W phase has lower

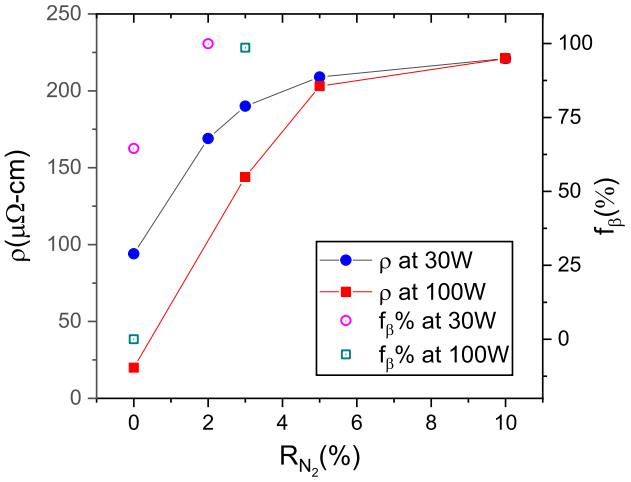

Fig. 6 Resistivity and volume fraction of β-W as a function of R_{N_2} at $P_W = 30$ *W* and 100 *W*

electrical resistivity in the range of 10–30 μΩ-cm, whereas the β-W phase is distinguished by relatively higher resistivity in the range of 150–300 μΩ-cm [12, 14]. Due to a large difference in resistivity of both the W phases, resistivity measurements have been employed in literature to know/conclude the type of W phase (dominant W phase) present in the film [9, 17, 19]. Figure 6 shows the variation of resistivity and f_β% as a function of nitrogen partial pressure for all the films. It is evident from Fig. 6 that resistivity increases with an increase in nitrogen partial pressure at both powers.

Further, it is observed that the resistivity of films with pure/dominant α-W phase is lower than the resistivity of films with pure/dominant β-W phase. For instance, the resistivity of films deposited at 100 *W* with $R_{N_2} = 0\%$, 5×10^{-7} torr N_2 and $R_{N_2} = 3\%$ is 20, 86 and 144 μΩ-cm, respectively. Resistivity of films deposited at higher R_{N_2} of 5% and 10% (i.e., amorphous films) is found to be higher than the crystalline films. Higher resistivity of β-W phase may be attributed to A-15 crystal structure, impurities, and crystallite size [45]. In our case, it can be concluded that resistivity is increasing both with an increase in R_{N_2} and f_β. As mentioned earlier the crystallite size of β-W phase is larger than that of both the α-W phase and the mean free path of electrons for tungsten (19 nm) [46]. Therefore, the A-15 crystal structure and nitrogen impurities seem to be the main source of the high resistivity of β-W phase. The resistivity behavior agrees well with the XRD results.

3.2 Effect of annealing

Annealing is a useful way to boost the performance of spintronic devices and materials. Spintronic devices such as SOT-MRAM that incorporate MTJs are required to be annealed up to 350–400 °C for improving the tunnel magnetoresistance (TMR) ratio [10]. The β-W is a promising SOT material and usually transform to α-W phase above room temperature depending upon film thickness [19, 20]. Therefore, it is important to examine the thermal stability of W films. Films with pure α-W phase and dominant β-W phase ($f_\beta = 98.6\%$) deposited at 100 *W* using $R_{N_2} = 0\%$ and 3%, respectively, are annealed in the range of 200–400 °C isochronally for 1 h. Figure 7 displays the XRD pattern of α-W film before and after annealing at 200–400 °C (deposited at $R_{N_2} = 0\%$ and 100 *W*).

It can be seen that α-W phase is observed for as-deposited and annealed films. No appreciable change in lattice parameter and crystallite size is observed after annealing upto 400 °C in this film and agrees well with the literature [20, 47, 48]. Crystallite size is not expected to change after annealing process, because no grain growth occurs after its nucleation. Resistivity of both as-deposited and 400 °C annealed film is found to be constant i.e., ~ 20 μΩ-cm. It indicates that resistivity measurements agree well with the XRD findings.

Figure 8a displays the XRD pattern of β-W film (majority phase) deposited at $R_{N_2} = 3\%$ at 100 *W* and annealed at 200–400 °C. The f_β of the as-deposited β-W film determined by XRD analysis (see Fig. 5a) is 98.6%. It is evident from Fig. 8a that there are no apparent differences in the XRD pattern of as-deposited and 200 °C annealed films except for slight shifting of all peaks towards a higher angle. However, using the fitting procedure, it is found that f_β decreases to 96.3% (see Fig. 8b). At annealing temperature of 300 °C, there is an appearance of a shoulder in the peak located around $2\theta = 40°$ and also a new peak at $2\theta = 73.25°$ corresponding to α(211) is observed. Further, it is evident from Fig. 8b that f_α has increased. The calculated f_α and f_β is

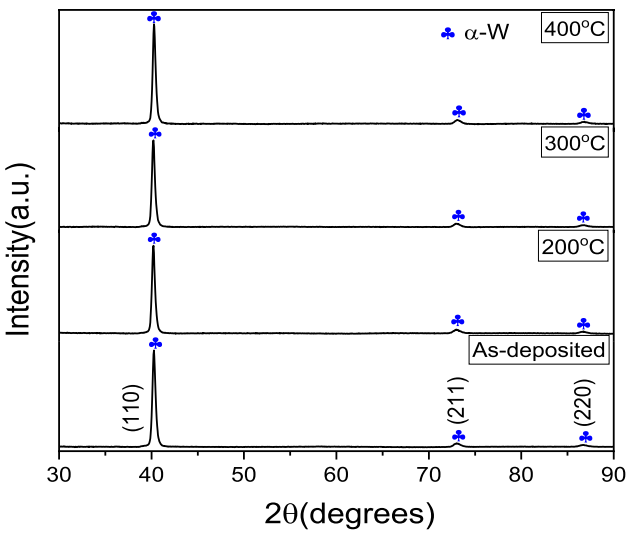

Fig. 7 XRD pattern of α-W film deposited at $P_W = 100$ *W*, $R_{N_2} = 0\%$ and annealed at 200–400 °C

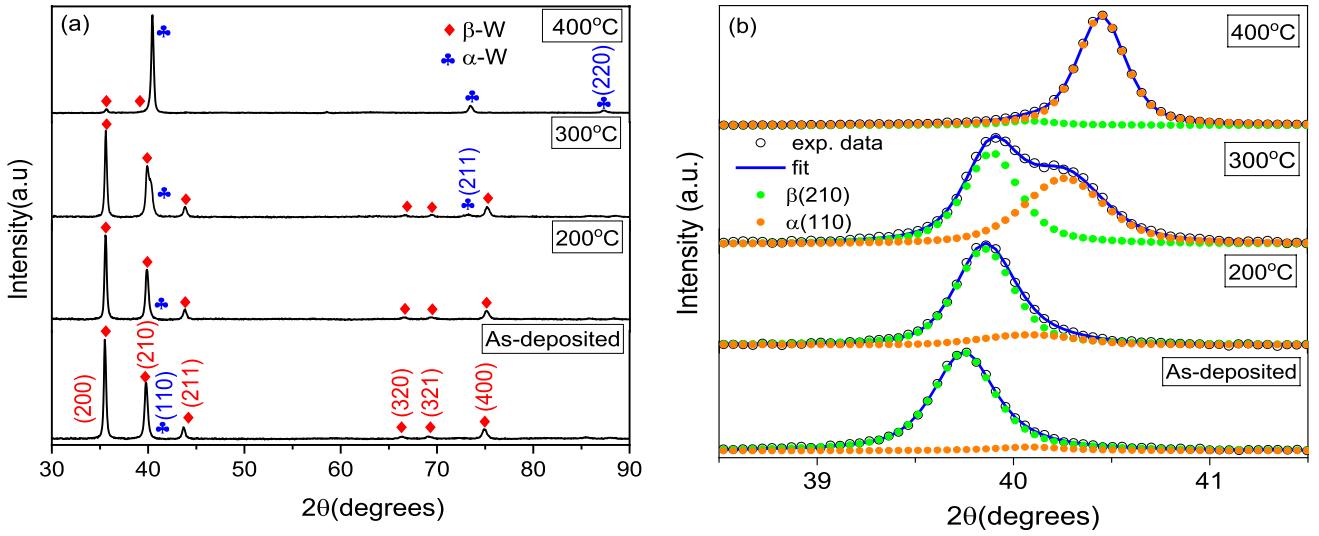

Fig. 8 **a** XRD pattern of the β-W film (majority phase) deposited at $P_W = 100$ *W*, $R_{N_2} = 3\%$ and annealed at 200–400 °C. **b** Fitting of the peak around $2\theta = 40^o$ shows that the f_β decreases as the annealing temperature increases from 200 to 400 °C

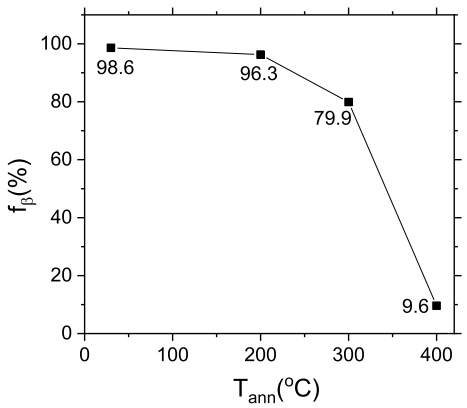

Fig. 9 Volume fraction of β-W(f_β) as a function of annealing temperature (T_{ann}) at $R_{N_2} = 3\%$ and $P_W = 100$ *W*

20.1% and 79.9%, respectively. As the annealing temperature is raised to 400 °C, intensity of β(200) peak decreases drastically and three additional peaks are observed at $2\theta = 40°$, 73.49°, 87.36° and are indexed as α(110)/β(210), α(211), α(220). Fitting of these peaks indicates the coexistence of both α and β phases after annealing at 400 °C, where α-W phase is dominant. In 400 °C annealed film the calculated $f_\beta = 9.6\%$; the decrease in f_β after 300–400 °C annealing is expected due to β-W → α-W phase transition. Variation of β-W phase fraction (f_β) with annealing temperature is shown in Fig. 9.

Resistivity is found to decrease from 144 to 40 μΩ-cm after thermal annealing at 400 °C in comparison to as-deposited film. The decrease in resistivity after annealing at 400 °C is due to the presence of the dominant α-W phase as observed in XRD. Thermal annealing at 400 °C does not completely transform β-W into α-W phase, which points towards the thermal stability of β-W phase. Stability of β-W at higher temperatures and for increasing thicknesses is a cause for concern for its incorporation into spintronic devices. Kaidatzis et al. observed the β → α phase transition in W films of $t \geq 10$ nm grown by dc sputtering technique at an annealing temperature of > 200 °C [19]. Similarly, Kim et al. reported that β-W films of t > 7 nm deposited by dc sputtering transform to α + β/α-W at an annealing temperature of 250 °C or higher [20]. In the abovementioned works, β-W films have been grown at a deposition rate of < 3 nm/min. The experiments in the present work show that β-W films of thickness as high as 70 nm deposited at a deposition rate of 3.13 nm/min are stable up to a temperature of 300 °C.

4 Conclusions

In this work, we report the dependence of W phase formed (α-W, β-W) on nitrogen partial pressure sputtering power, and annealing temperature in 50–70 nm thick W films. It is observed that with an increase in nitrogen partial pressure (R_{N_2}) from 0 to 10% the deposition rate, W film density and surface roughness decreases at both the powers. Tungsten film density match with bulk tungsten's density (19.31 g/cm^3) at $R_{N_2} = 0\%$, and it falls to 17.85(17.91) at $R_{N_2} = 10\%$ for 30 *W* (100 *W*). XRD analysis shows that at $R_{N_2} = 0\%$ the tungsten film contains mixed/pure α-W phase at 30 *W*/100 *W*, indicating the dependence of W-phase formation at deposition power (deposition rate). The $R_{N_2} = 2\%$ stabilizes β-W at $P_W = 30$ *W* ($\Gamma = 0.91$ nm/min), however higher R_{N_2} of 3% is

required to stabilize β-W at $P_W = 100$ *W* ($\Gamma = 3.13$ nm/min). At $P_W = 100$ *W*, it is found that 5×10^{-7} torr N_2 is sufficient to transform the fraction of α-W to β-W phase ($f_\beta\% = 33.4$). At higher power, higher nitrogen concentration/partial pressure is required to increase the probability of interaction between W atoms/clusters and nitrogen ions to stabilise the β-W phase. It is because of the fact that at a higher deposition rate, the probability of interaction of sputtered W atoms/clusters with surrounding oxygen and nitrogen ions is lower. Electrical resistivity measurements show that resistivity rises with an increase in nitrogen partial pressure at both powers. In the case of films deposited at 100 *W* with $R_{N_2} = 0$ and 3%, the resistivity is found to be 20 μΩ-cm (α-W) and 144 μΩ-cm (β-W) respectively, which agrees well with XRD results. The α-W films deposited at $R_{N_2} = 0\%$ and 100 *W* is found to be stable upto 400 °C indicating the thermal stability of α-W phase. The ~ 70 nm thick β-W films deposited at $R_{N_2} = 3\%$ and $P_W = 100$ *W* are thermally stable upto 300 °C as the majority phase with $f_\beta \sim 80\%$, and even at 400 °C a complete transformation to pure α-W phase is not observed.

In summary, we demonstrate the stabilization of β-W phase in 70 nm thicker W films at a relatively higher deposition rate of 3.13 nm/min as compared to earlier works. Further, the surface roughness and mass density values of β-W films indicate that our films are smoother and less porous than reported in literature. Stabilization of β-W phase at a higher deposition rate with lower surface roughness and porosity could be beneficial for mass-scale production and better performance of spintronics devices including SOT-MRAM.

Supplementary Information The online version contains supplementary material available at https://doi.org/10.1007/s00339-023-06552-x.

Acknowledgements Technical support from Ms. Susmita Chowdhury (DAVV, Indore) in thin film deposition, Mr. Layanta Behera (UGC-DAE CSR, Indore) in thermal annealing and XRD measurements, Ms. Ratnawali Verma (DAVV, Indore) for performing resistivity measurements is highly acknowledged. Dr. Dileep Kumar (UGC-DAE CSR, Indore) is acknowledged for providing a resistivity measurement facility. H.S. acknowledges the Ministry of Education (MoE), Government of India for providing the senior research fellowship.

Author contributions HS: conceptualization; data curation; formal analysis; investigation, writing- original draft. MG: conceptualization; resources; formal analysis; review and editing. PG: resources; data curation. RFSP: investigation; formal analysis. SLM: investigation; formal analysis. HK: conceptualization; formal analysis; investigation; writing- review and editing; supervision.

Data availability The data generated during the current study are available from the corresponding author upon reasonable request.

Declarations

Conflict of interest The authors declare they have no conflict of interest.

References

1. S.M. Rossnagel, I.C. Noyan, C. Cabral Jr., J. Vac. Sci. Technol. B **20**, 2047 (2002)
2. N. Radić, A. Tonejc, J. Ivkov, P. Dubček, S. Bernstorff, Z. Medunić, Surf. Coat. Technol. **180–181**, 66 (2004)
3. T. Salditt, T. D. Lott, T. H. Metzger, J. Peisl, G. Vignaud, P. Ho/gho/j, O. Schärpf, P. Hinze, and R. Lauer, Phys. Rev. B, **54,** 5860 (1996).
4. M. Itoh, M. Hori, S. Nadahara, J. Vac. Sci. Technol. B **9**, 149 (1991)
5. E. Grigore, M. Gherendi, F. Baiasu, M. Firdaouss, C. Hernandez, A. Weckmann, P. Petersson, A. Hakola, Fusion Eng. Des. **146**, 1959 (2019)
6. M. Rieth, S.L. Dudarev, S.M. Gonzalez de Vicente, J. Aktaa, T. Ahlgren, S. Antuscha, D.E.J. Armstrong et al., J. Nucl. Mater. **432**, 482 (2013)
7. J.A. Hofer, N. Haberkorn, Thin Solid Films **685**, 117 (2019)
8. C.F. Pai L. Liu, Y. Li, H. W. Tseng, D. C. Ralph, and R. A. Buhrman, Appl. Phys. Lett. **101**, 122404 (2012).
9. Q. Hao, W. Chen, G. Xiao, Appl. Phys. Lett. **106**, 182403 (2015)
10. T.Rahman, J. Pellegren, A. Smith, C. Wiegand, N. Sato, T. Gosavi, *et al*., (2021). U.S. Patent No. 11, 062,752 (13 July 2021)
11. H. Mazraati, S. Chung, A. Houshang, M. Dvornik, L. Piazza, F. Qejvanaj, S. Jiang, T.Q. Le, J. Weissenrieder, J. Åkerman, Appl. Phys. Lett. **109**, 242402 (2016)
12. P. Petroff, T.T. Sheng, A.K. Sinha, G.A. Rozgonyi, F.B. Alexander, J. Appl. Phys. **44**, 2545 (1973)
13. I.A. Weerasekera, S.I. Shah, D.V. Baxter, K.M. Unruh, Appl. Phys. Lett. **64**, 3231 (1994)
14. M.J. O'Keefe, J.T. Grant, J.S. Solomon, J. Electron. Mater. **24**, 961 (1995)
15. D. Choi, Microelectron. Eng. **183–184**, 19 (2017)
16. J.S. Lee, J. Cho, C.-Y. You, J. Vac. Sci. Technol. A **34**, 021502 (2016)
17. C. Zhang, S. Fukami, K. Watanabe, S. DuttaGupta, H. Sato, F. Matsukura, H. Ohno, Appl. Phys. Lett. **109**, 192405 (2016)
18. R. Bansal, G. Nirala, A. Kumar, S. Chaudhary, P.K. Muduli, Spin **8**, 1850018 (2018)
19. A. Kaidatzis, V. Psycharis, K. Mergia, D. Niarchos, Thin Solid Films **619**, 61 (2016)
20. Y. J. Kim S. G. Kang, Y. Oh, G. W. Kim, I. H. Cha, H. N Han, and Y. K. Kim, Materials Characterization **145**, 473 (2018).
21. W. Chen, G. Xiao, Q. Zhang, X. Zhang, Phys. Rev. B **98**, 134411 (2018)
22. J.-C. Rojas-Sánchez, N. Reyren, P. Laczkowski, W. Savero, J.-P. Attané, C. Deranlot, M. Jamet, J.-M. George, L. Vila, H. Jaffrès, Phys. Rev. Lett. **112**, 106602 (2014)
23. L.Q. Liu, C.F. Pai, Y. Li, H.W. Tseng, D.C. Ralph, R.A. Buhrman, Science **336**, 555 (2012)
24. A. Chattaraj, M. Patidar, V. Ganeshan, S. Joulie, V. Serin, A. Claverie, V. Kumar, A. Kanjilal, J. Material Res. **37**, 4338 (2022)
25. J.A. Hofer, N. Haberkorn, Thin Solid Films **730**, 138690 (2021)
26. J.A. Hofer, S. Bengio, S. Suárez, N. Haberkorn, Mater. Adv. **4**, 150 (2023)
27. F.T.N. Vullers, R. Spolenak, Thin Solid Films **577**, 26 (2015)
28. K. Salamon, O. Milat, N. Radić, P. Dubček, M. Jerčinović, S. Bernstorff, J. Phys. D, Appl. Phys. **46**, 095304 (2013)
29. A. Chattaraj, J. Asirvatham, G. Das, G. Manna, P. Saha, V. Kumar, A. Kanjilal, J. Appl. Phys. **131**, 125301 (2022)
30. M. Arita, I. Nishida, Jpn. J. Appl. Phys. **32**, 1759 (1993)
31. Y.G. Shen, Y.W. Mai, Mater. Sci. Eng. A **284**, 176 (2000)
32. L. Maillé, C. Sant, C. Le Paven-Thivet, C. Legrand-Buscema, P. Garnier, Thin Solid Films **428**, 237 (2003)

33. A.J. Narasimham, M. Medikonda, A. Matsubayashi, P. Khare, H. Chong, R.J. Matyi, A. Diebold, V.P. LaBella, AIP Adv. **4**, 117139 (2014)
34. J. Liu, K. Barmak, Acta Mater. **104**, 223 (2016)
35. K. Hon, S. Couet, K.K.V. Sethu, J. Swerts, G.S. Kar, Thin Solid Films **732**, 138795 (2021)
36. S. Ikeda K. Miura, H. Yamamoto, K. Mizunuma, H.D. Gan, M. Endo, S. Kanai, J. Hayakawa, F. Matsukura, and H. Ohno, A, Nat. Mater**. 9** 721 (2010).
37. C. Braun, Parratt32- The Reflectivity Tool, HMI, Berlin, 1997–1999.
38. A.H. Abdelhameed, W. Jacob, Sur. Coat. Technol. **37**, 701 (2019)
39. S. Kalal, M. Gupta, R. Rawat, J. Alloy. Compd. **851**, 155925 (2021)
40. R. Gupta, M. Gupta, Phys. Rev. B **72**, 024202 (2005)
41. K. Barmak and J. Liu, J. Vac. Sci. Technol. A, **35**, 061516 (2017).
42. D. Jhajhria, N. Behera, D.K. Pandya, S. Chaudhary, Phys. Rev. B **99**, 014430 (2019)
43. S.N. Panda, S. Majumder, A. Bhattacharyya, S. Dutta, S. Choudhury, A. Barman, A.C.S. Appl, Mater. Interfaces **13**, 20875 (2021)
44. A.J. Narasimham, A. Green, R.J. Matyi, P. Khare, T. Vo, A. Diebold, V.P. LaBella, AIP Adv. **5**, 117107 (2015)
45. D. Choi, B. Wang, S. Chung, X. Liu, A. Darbal, A. Wise, N.T. Nuhfer, K. Barmak, J. Vac. Sci. Technol. A **29**, 051512 (2011)
46. D. Choi, C.S. Kim, D. Naveh, S. Chung, A.P. Warren, N.T. Nuhfer, M.F. Toney, K.R. Coffey, K. Barmak, Phys. Rev. B **86**, 045432 (2012)
47. G.S. Chen, L.C. Yang, H.S. Tian, C.S. Hsu, Thin Solid Films **484**, 83 (2005)
48. X. Liu, D. Choi, H. Beladi, N.T. Nuhfer, G.S. Rohrer, K. Barmak, Scripta Mater. **69**, 413 (2013)